Dynamics in the Mn^{2+} Binding Site in Single Crystals of Concanavalin A Revealed by High-Field EPR Spectroscopy†

Raanan Carmieli,‡ Palanichamy Manikandan,‡ Boris Epel,‡ A. Joseph Kalb (Gilboa),§ Alexander Schnegg,|| Anton Savitsky,|| Klaus Möbius,|| and Daniella Goldfarb*,‡

Departments of Chemical Physics and Structural Biology, The Weizmann Institute of Science, Rehovot, Israel 76100, and Department of Physics, Freie University Berlin, Arnimallee 14, 14195 Berlin, Germany

Received February 19, 2003; Revised Manuscript Received April 25, 2003

ABSTRACT: EPR spectroscopy at 95 GHz was used to characterize the dynamics at the Mn^{2+} binding site in single crystals of the saccharide-binding protein concanavalin A. The zero-field splitting (ZFS) tensor of the Mn^{2+} was determined from rotation patterns in the *a*−*c* and *a*−*b* crystallographic planes, acquired at room temperature and 4.5 K. The analysis of the rotation patterns showed that while at room temperature there is only one type of Mn^{2+} site, at low temperatures two types of Mn^{2+} sites, not related by any symmetry, are distinguished. The sites differ in the ZFS parameters *D* and *E* and in the orientation of the ZFS tensor with respect to the crystallographic axes. Temperature-dependent EPR measurements on a crystal oriented with its crystallographic *a* axis parallel to the magnetic field showed that as the temperature increases, the two well-resolved Mn^{2+} sextets gradually coalesce into a single sextet at room temperature. The line shape changes are characteristic of a two-site exchange. This was confirmed by simulations which gave rates in the range of 10^7-10^8 s^{-1} for the temperature range of 200−266 K and an activation energy of 23.8 kJ/mol. This dynamic process was attributed to a conformational equilibrium within the Mn^{2+} binding site which freezes into two conformations at low temperatures.

Conformational dynamics in proteins is an extensively studied field of research because of its relation to functional behavior of proteins. Although X-ray diffraction methods are not among the most effective methods for identifying and characterizing conformational equilibria, the existence of such processes can be inferred from analysis of thermal factors and multiple crystal forms (*1*, *2*). The latter are attributed to lattice energies which may be large enough for selection of a particular conformation over the other. In contrast, NMR[1] spectroscopy is one of the most effective methods for studying protein dynamic equilibria in solution, and this is accomplished primarily through measurements of relaxation times (*3*, *4*). Conformational dynamics in lyophilized and polycrystalline proteins is best followed by solid state NMR, where both relaxation measurements of various nuclei and ^2H line shape analysis are employed (*5*−*8*). Other commonly used methods are EPR and fluorescence spectroscopy, which usually require the introduction of a spin-label (*9*) or a chromophore through chemical modifications (*10*). Sometimes, the protein consists of an inherent paramagnetic center, which can be used as an intrinsic probe for EPR spectroscopy, such as the quinone radical anions in the photosynthetic bacterial reaction center (*11*).

High-field EPR and electron−nuclear double-resonance (ENDOR) spectroscopy have been shown to be most instrumental in the studies of structural aspects of metalloproteins, both in frozen solutions (*12*−*14*) and in single crystals (*15*−*17*). The latter has become possible due to the high sensitivity of high-field EPR to size-limited samples. Single-crystal studies on Cu(II) in azurin (*15*) and nitrite reductase (*18*) provided the orientation of the **g**-tensor. ENDOR measurements of azurin (*16*) revealed an unexpected number of weakly coupled nitrogens in the Cu(II) site, and their ^{14}N hyperfine and quadrupole tensors were determined. In addition, single-crystal electron-spin-echo envelope modulation (ESEEM) measurements provided these tensors for the directly bound ^{14}N nuclei. Finally, ENDOR measurement of single crystals of concanavalin A gave the coordinates of water and imidazole protons in the binding site of Mn^{2+} (*17*). Here we show that the high resolution and sensitivity of the high-field Mn^{2+} EPR spectrum can be harnessed to detect and characterize dynamics processes at the metal site in single crystals of the protein concanavalin A.

Concanavalin A is a member of the plant hemagglutinin (or plant lectin) family, a large and ubiquitous group of saccharide-binding proteins whose biological function is as

† This research was supported by the DFG Schwerpunkt program "High field EPR in Physics, Chemistry and Biology" and by the The Ilse Katz Institute for Material Sciences and Magnetic Resonance Research.

* To whom correspondence should be addressed. Telephone: 972-8-9342016. Fax: 972-8-9344123. E-mail: daniella.goldfarb@weizmann.ac.il.

‡ Department of Chemical Physics, The Weizmann Institute of Science.

§ Department of Structural Biology, The Weizmann Institute of Science.

|| Freie University Berlin.

[1] Abbreviations: EPR, electron paramagnetic resonance; NMR, nuclear magnetic resonance; ZFS, zero-field splitting; ENDOR, electron−nuclear double resonance; ESEEM, electron-spin-echo envelope modulation; CW, continuous wave; DPPH, 2,2-diphenyl-1-picrylhydrazyl; RT, room temperature; XRD, X-ray diffraction.

10.1021/bi034281+ CCC: $25.00
Published on Web 06/12/2003

yet unknown (*19*). The importance of these proteins is expressed in their ability to bind saccharides; each member of the family has a unique saccharide specificity (*19*). The three-dimensional (3D) structure of concanavalin A has been determined at 110 K at an exceptionally high resolution of 0.94 Å (*21*). The overall structure of the protein dimer is dominated by an extensive β-sheet strand arrangement, the so-called jellyroll motif. This further associates as a dimer of dimers to form a tetramer with a total molecular mass of 100 kDa. Each monomer contains two metal binding sites, the occupancy of which is essential for saccharide binding (*20*). The first site, called S1, is occupied by a transition metal ion, e.g., Mn^{2+}, and Ca^{2+} resides in the second site, termed S2. The Mn^{2+} ion has a slightly distorted octahedral geometry in which it is coordinated to the carboxyl groups of Asp10, Asp19, and Glu8, the imidazole N_ϵ of His24, and two water molecules. The carboxyl groups of Asp10 and Asp19 form a bridge to the Ca^{2+}. The role of the transition metal in this protein is structural; namely, the Mn^{2+} and the Ca^{2+} serve as stabilizers for the loops that constitute the saccharide binding site. The crystal has orthorhombic symmetry (space group I_{222}), with the following unit cell parameters: $a = 89.2$ Å, $b = 87.2$ Å, and $c = 62.9$ Å.

In this work, we present the results of a temperature-dependent W-band EPR study on single crystals of concanavalin A. Two Mn^{2+} sites with ZFS tensors differing in both the magnitude of the principal components and the orientation with respect to the crystallographic axes were detected at low temperatures. In contrast, only one type was found to exist at room temperature. The EPR line shape evolution with temperature showed the existence of a two-state conformational equilibria above 200 K.

EXPERIMENTAL PROCEDURES

The crystals were grown and mounted as described previously (*17*). They have a well-defined morphology, where their long dimension coincides with the *b* axis. Continuous wave (CW) EPR spectra were collected using a home-built spectrometer operating at 94.9 GHz (*24*). The design of the CW probe head was based on that of the Berlin group (*25*). Magnetic field modulation, at a frequency of 100 kHz, was achieved by a copper coil of 100 turns that provides a maximum modulation amplitude of ~12 G. In the CW setup, the output of the phase sensitive detector is fed into a lock-in amplifier (Stanford Research Systems model SR850) that is interfaced with a personal computer. The magnetic field was calibrated using a sample of DPPH which was glued to one of the cavity flanges. The temperature was controlled using a Janis model STVP-200 "Supertran" variable-temperature insert (VTI) with a Lakeshore controller and two temperature sensors, one located near the heater and the other on the probe head, close to the cavity. Rotation patterns in two crystallographic planes ($a-c$ and $a-b$) where collected at room temperature and 4.5 K. A crystal was first oriented with its *b* axis perpendicular to the magnetic field, $\vec{B}$, and a rotation pattern was collected in the $a-c$ plane; then the crystal was rapidly cooled inside the probe head using the Janis cryostat setup, and a rotation pattern was collected at 4.5 K. This procedure was repeated for a crystal oriented with the *c* axis perpendicular to the magnetic field. In addition, a crystal oriented with field $\vec{B}$ parallel to the *a* axis was subjected to temperature-dependent measurements, where the temperature was increased stepwise from 4.5 to 265 K. We have checked that the cooling procedure yields the same spectra that were obtained by rapid immersion into liquid nitrogen as reported previously (*17*). CW EPR rotation patterns in the $a-c$ plane were also collected at 265 and 160 K on the Berlin 95 GHz spectrometer (*25*).

Simulations and Data Analysis. The spin Hamiltonian of $^{55}Mn^{2+}$ (d^5, $S = {}^5/_2$, $I = {}^5/_2$) is given by

$$\mathcal{H} = g\beta\vec{B}\hat{S}_Z - g_N\beta_N\vec{B}\hat{I}_Z + \hat{I}\cdot\mathbf{A}\cdot\hat{S} + \hat{S}\cdot\mathbf{D}\cdot\hat{S} \qquad (1)$$

where the first and second terms correspond to the electron and nuclear Zeeman interactions, respectively, the third term corresponds to the ^{55}Mn hyperfine interaction, and the fourth term corresponds to the ZFS. Since **D** is traceless, the ZFS term can be expressed with just two parameters as follows:

$$\hat{S}\cdot\mathbf{D}\cdot\hat{S} = \frac{D}{3}[3\hat{S}_z'^2 - S(S+1)] + E(\hat{S}_x'^2 - \hat{S}_y'^2) \qquad (2)$$

where $D = {}^3/_2D_{zz}$, $E = D_{yy} - D_{xx}$, and the coordinates *x*,*y*,*z* refer to the principal axis system of the ZFS tensor.

When $D \ll g\beta B_0$, second-order perturbation theory yields the following resonant magnetic fields for the $|-{}^1/_2, m\rangle \rightarrow |{}^1/_2, m\rangle$ transitions (*22*):

$$B({}^1/_2, m) = B_0 - \frac{mA}{g\beta} + f(D,E,\theta,\phi) - mF \qquad (3)$$

where

$$f(D,E,\theta,\phi) = \frac{16}{g\beta B_0}\{(D - E\cos 2\phi)^2 \sin^2\theta\cos^2\theta + E^2\sin^2 2\phi\sin^2\theta - {}^1/_8[D\sin^2\theta + E\cos 2\phi(1+\cos^2\theta)]^2 - {}^1/_2E^2\cos^2\theta\sin^2 2\phi\} \qquad (4)$$

m is the ^{55}Mn nuclear spin state, *A* is the ^{55}Mn hyperfine coupling constant, and *F* includes cross terms between the ZFS and the hyperfine interaction on the order of $AD^2/(g\beta B_0)^2$. The angles θ and ϕ give the orientation of the magnetic field with respect to the principal axis system of **D**.

The EPR rotation patterns were simulated using a computer program based on eq 3, and the best fit was determined using the E04FYF routine of the NAG library. The fitting procedure was carried out on the experimentally acquired rotation patterns of two crystallographic planes. Since **D** is traceless and the symmetry relation between the four Mn^{2+} sites is known, the components of **D** can be uniquely determined from rotation patterns in two crystallographic planes (*22*). For convenience, the following reference frames were used: the principal axis system of the ZFS tensor, $P(x,y,z)$, the crystal frame $C(c,a,b)$ (*22*), the sample tube frame $T(x',y',z')$, where z' is parallel to the tube axis, the goniometer frame $G(x'',y'',z'')$, and the lab frame $B(X,Y,Z)$, where *Z* is parallel to $\vec{B}$. The transformation between these axes systems is described via the appropriate Euler angles, and the ZFS tensor transformations are carried out using the corresponding Wigner rotation matrices, $R(\alpha',\beta',\gamma')$. For our experimental setup, the transformations are

$$P \xrightarrow{\alpha,\beta,\gamma} C \xrightarrow{\phi',\theta',\psi} T \xrightarrow{0,0,\phi_0} G \xrightarrow{\phi_r,90,0} B \qquad (5)$$

Table 1: Euler Angles Relating the Principal Axis System of the ZFS Tensor with the Crystallographic Axis System for the Four Different Crystallographic Mn^{2+} Sites of Concanavalin A

site I	α	β	γ
site II	α	β	$\gamma + 180°$
site III	$180° + \alpha$	$180° - \beta$	$180° - \gamma$
site IV	$180° + \alpha$	$180° - \beta$	$-\gamma$

The rotation patterns were acquired by measuring the spectrum as a function of the rotation angle of the goniometer, ϕ_r. The relation between the above sets of angles and the angles θ and ϕ in eq 3 is given by

$$R(0,\theta,\phi) = R(\alpha,\beta,\gamma)R(\phi',\theta',\psi)R(0,0,\phi_0)R(\phi_r,90°,0) \quad (6)$$

All angles in eq 6, besides α, β, and γ, are defined by the experimental conditions. There are four Mn^{2+} centers per unit cell in the crystals of concanavalin A (*21*), and according to the I_{222} space group, their α, β, and γ angles are related as described in Table 1. The values of D, E/D, A, α, β, and γ for each site were obtained from best fit simulations of the rotation patterns of the $|-1/2, 5/2\rangle \rightarrow |1/2, 5/2\rangle$ transition [assuming a negative A (^{55}Mn)]. To display the orientation of the ZFS, determined relative to the $C(c,a,b)$ axis system, in the atomic coordinate system (c,b,a) (*21*) (as shown in Figure 6), an additional transformation of $R(-90°,90°,90°)$ was carried out.

RESULTS

A single crystal of concanavalin A, with a well-defined morphology (*17*), was oriented with its c axis parallel to the sample tube axis (perpendicular to the direction of the external magnetic field), and W-band CW EPR spectra were recorded as a function of the orientation of the magnetic field, ϕ_r, in the crystallographic $a-b$ plane. High resolution was observed only in the region of the central $|-1/2, m\rangle \rightarrow |1/2, m\rangle$ EPR transitions. The broadening of the other transitions is attributed to the presence of a distribution in the D and E values (*22*). These transitions are more susceptible to such broadening due to their first-order dependence on the ZFS parameters, as opposed to a second-order contribution for the central transitions. Room-temperature (RT) spectra are shown in Figure 1. The region shown corresponds to the high-field half of the six ^{55}Mn hyperfine lines of the $|-1/2, m\rangle \rightarrow |1/2, m\rangle$ EPR transitions. The low-field half is not shown because part of it overlaps with the intense DPPH signal. The spectra exhibit two well-resolved sets of sharp sextets of the spectroscopically distinct Mn^{2+} sites in this plane. At ϕ_r values of 5° and 95°, the sextets of the two sites merge, indicating that the magnetic field is along one of the crystallographic axes. The change in the signal intensity is due to variations in the tuning conditions caused by the rotation of the crystal. Similar measurements were carried out in the $a-c$ plane. The $a-b$ and $a-c$ rotation patterns of the highest-field hyperfine component are displayed in Figure 2. Best fit simulations of the rotation patterns, using the relation between the crystallographic sites given in Table 1, are presented by the solid lines in Figure 2. The best fit parameters of one of the sites are given in Table 2. The procedure used for the identification of the crystallographic axes is described later.

The values we obtained for the ZFS tensor at room temperature differ somewhat from those determined by earlier Q-band measurements (see Table 2) (*22*), with the difference in E/D being the most significant. Introduction of the Q-band-determined parameters to our simulations produced a fit that was reasonable, but not as good as the one obtained with our parameters. We attribute the discrepancy to experimental error originating from differences in data quality; at W-band, data were collected with a rotation angle in the range of 0−180°, every 5°, whereas at Q-band, data were recorded in the range of 10−170°, each 10°. The larger range and number of points lead to more accurate results.

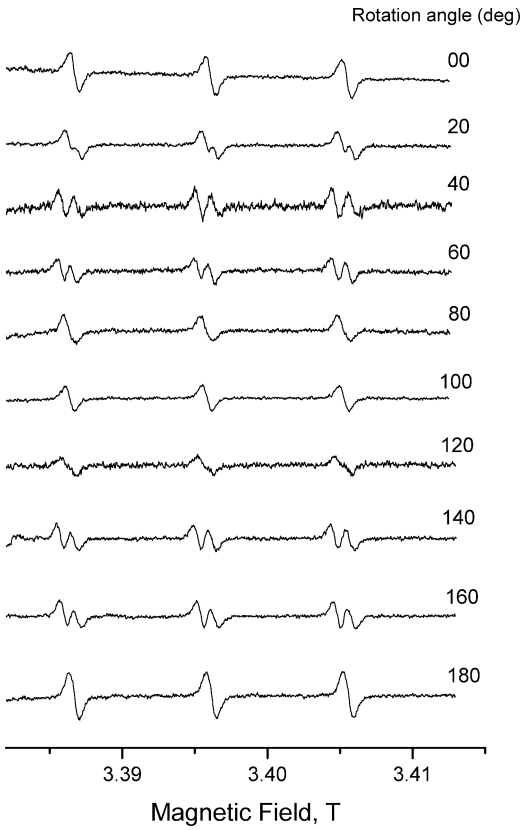

FIGURE 1: CW W-band EPR spectra of a single crystal of concanavalin A in the $a-b$ plane recorded at RT.

CW EPR spectra recorded at 4.5 K for different orientations within the $a-b$ plane are shown in Figure 3. At a rotation angle of 5°, only one sextet is observed, thus suggesting this direction as one of the crystallographic axes. A 90° rotation to 95° should therefore place the magnetic field along another crystallographic axis, where again a single sextet is expected. In contrast, the spectrum exhibits two sextets. Moreover, in some other orientations within this plane, it is possible to identify three or four different sextets (see, for example, the 40° and 140° traces). Similarly, some spectra acquired in the $a-c$ plane show more than two sextets, and when $\vec{B}$ is parallel to the a axis, two sextets are clear, thus suggesting that more than one type of Mn^{2+} site is present. The 4.5 K CW EPR rotation patterns of the highest-field line of the sextets in the $a-c$ and $a-b$ planes are depicted in Figure 4. The RT and low-temperature rotation patterns were measured on the same crystal. Best fit simulations of the rotation patterns are depicted as the solid lines in Figure 4, and the parameters that were used are listed in Table 2. The regions with missing experimental points are due to the limited resolution. The analysis of the

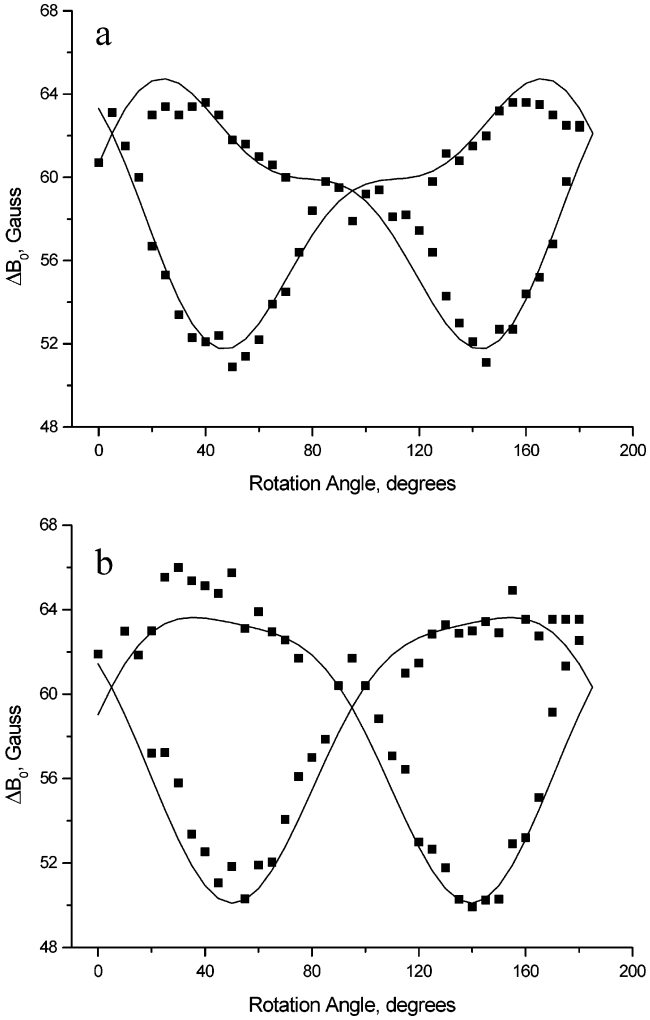

FIGURE 2: Rotation pattern of the highest-field ^{55}Mn hyperfine component of a single crystal of concanavalin A measured at RT: (A) $a-b$ plane and (B) $a-c$ plane. The resonant magnetic field, ΔB_0, is given with respect to 3.4 T. The solid lines are the best fit simulated traces.

Table 2: Summary of the ZFS Parameters at Room Temperature and 4.5 K[a]

Mn^{2+} site	D (±10) (MHz)	E/D (±0.005)	α (±5) (deg)	β (±3) (deg)	γ (±5) (deg)
Mn^{2+} (RT)	726 (650)	0.115 (0.185)	96 (147)	58 (54)	45 (42)
Mn_A^{2+}	789	0.24	125	52	36
Mn_B^{2+}	970	0.145	50	56	58

[a] In all cases, the ^{55}Mn hyperfine coupling was 265 MHz. The values in parentheses are those obtained by Q-band EPR (*22*), after adapting them to our definition of order of rotations (from lab to ZFS as opposed to from ZFS to lab).

rotation patterns showed that there are two types of chemically inequivalent Mn^{2+} sites, termed $(Mn^{2+})_A$ and $(Mn^{2+})_B$. They have different D and E values as well as different orientations with respect to the crystallographic axes. Moreover, for each of these sites, two crystallographic sites are detected in the crystallographic planes, and their spectra merge into one when the field is along one of the crystallographic axes, just as expected for the I_{222} crystal symmetry. The site splitting in the simulated spectra was obtained from the relationships given in Table 1.

Field-sweep echo-detected EPR spectra recorded at 4.5 K were identical to those obtained by the CW EPR measurements. The identification of the EPR spectra corresponding to a particular crystallographic axis was based on earlier low-temperature pulsed ENDOR measurements, where ENDOR spectra were compared (*17*). Unfortunately, pulsed ENDOR measurements could not be carried out at RT because the observation of echoes requires cryogenic temperatures. Nonetheless, because the RT and low-temperature measurements were carried out on the same crystal, it was enough to determine the orientation at one temperature.

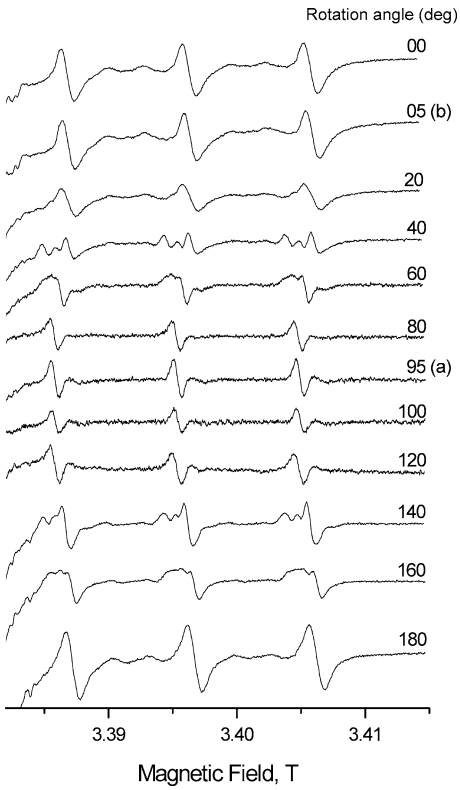

FIGURE 3: CW W-band EPR spectra of a single crystal of concanavalin A in the $a-b$ plane recorded at 4.5 K. The position of crystallographic axes *a* and *b* are noted next to the corresponding spectra.

The low-temperature measurements showed that while in the spectra recorded with $\vec{B}$ parallel to the *b* and *c* axes the two ^{55}Mn hyperfine sextets could not be resolved, with $\vec{B}$ parallel to the *a* axis two distinguished sextets were easily detected. Consequently, this crystal orientation was chosen for temperature-dependent EPR measurements in the range of 4.5−293 K. The spectra are presented in Figure 5A, where only the highest-field component of the sextet is depicted and an arbitrary relative field is used for the *X* axis to avoid using large numbers. In this experiment, the RT spectrum was first recorded, the crystal was then rapidly cooled to 4.5 K, and then measurements were performed by increasing the temperature. It is not possible to cool the crystal slowly past the freezing point as it cracks. Furthermore, during the heating process (from 4.5 K), it is not possible to reach room temperature because the crystal is damaged upon thawing. Because of these limitations, measurements in the region of 273 K were not performed. The spectra in Figure 5A show that up to 205 K there is no significant change and the spectrum can be simulated as a superposition of two lines with different widths and relative intensities. From 205 K and above, the separation between the lines decreases significantly, until they merge into a single line at RT. These

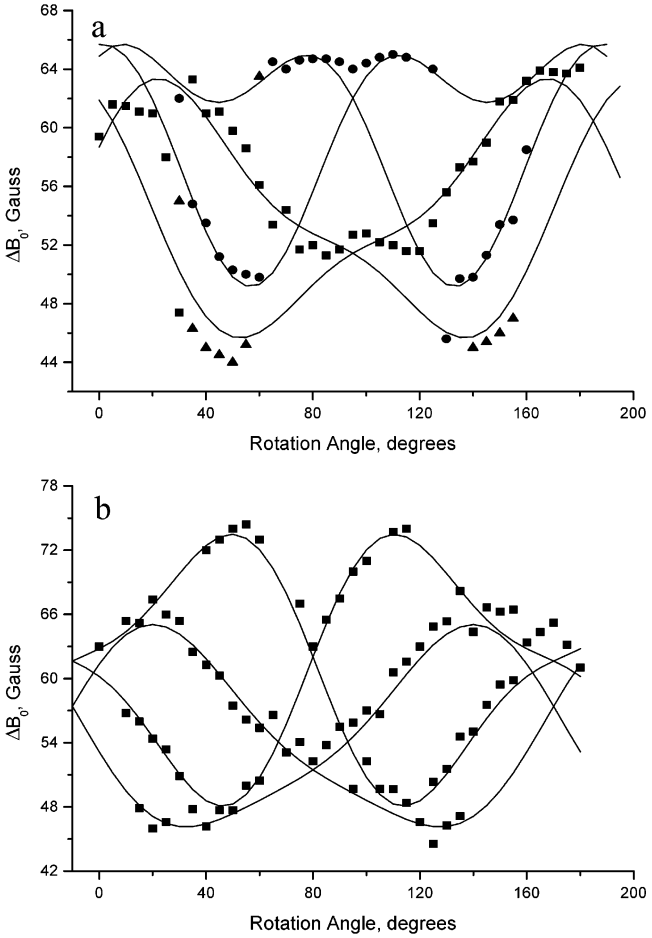

FIGURE 4: Rotation pattern of the highest-field ^{55}Mn hyperfine component of a single crystal of concanavalin A measured at 4.5 K: (A) $a-b$ plane and (B) $a-c$ plane. The resonant magnetic field, ΔB_0, is given with respect to 3.4 T. The solid lines are the best fit simulation traces.

line shape changes are typical for a dynamic process involving a two-site exchange. Indeed, the spectra could be simulated using the following simple process:

$$Mn_A^{2+} \underset{\tau_b^{-1}}{\overset{\tau_a^{-1}}{\rightleftharpoons}} Mn_B^{2+} \quad (7)$$

using the standard expressions (*28*). τ_a and τ_b are the rate constants, whereas the relative populations of Mn_A^{2+} and Mn_B^{2+} are given by f_a and f_b ($f_a + f_b = 1$). The difference in the resonant field positions is ΔB, and $1/\tau = 1/\tau_a + 1/\tau_b = k$. The simulated traces are depicted in Figure 5A, and the simulation parameters are summarized in Table 3. The simulations show that the rate constant increases with temperature, and at 266 K, it reaches 6×10^8 s^{-1}. The two states are not equally populated; at low temperatures, $f_a =$ 64%, whereas at 266 K, it decreases to 38%. In addition, the line widths of both decrease with temperature, with the width of Mn_A^{2+} being consistently lower than that of Mn_B^{2+}. An Arrhenius plot of the temperature dependence of k is shown in Figure 5B, yielding an activation energy of 23.8 kJ/mol and a ΔS_e of 3.2 kJ/mol for the entropy activation.

DISCUSSION

The experimental results showed that at low temperatures concanavalin A has two types of chemically inequivalent

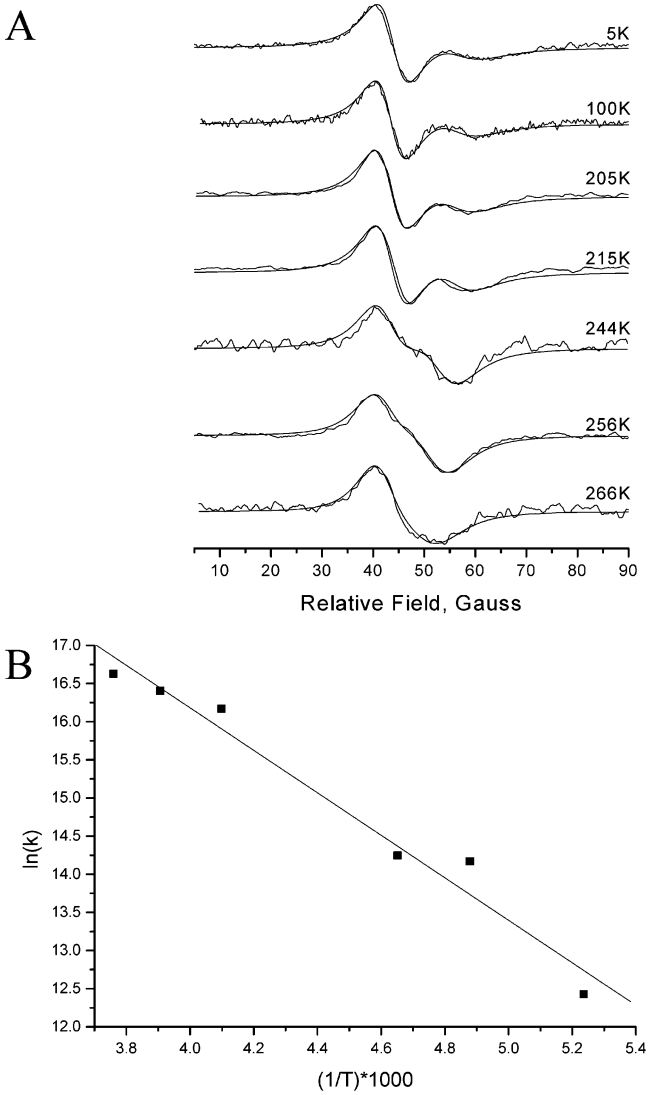

FIGURE 5: (A) Temperature dependence of the CW EPR spectra of a single crystal of concanavalin A oriented with B parallel to the a axis and simulations obtained with the parameters given in Table 3. Only the region of the highest-field ^{55}Mn hyperfine components is displayed. (B) Temperature dependence of k as determined from the simulation shown in panel A.

Table 3: Summary of the Parameters Obtained from the Simulations of the Temperature-Dependent Spectra Shown in Figure 5A

temp (K)	τ (s)	f_a	ΔB (G)	line width of A (G)	line width of B (G)
5	–	0.64	12.5	5.5	9.2
100	–	0.64	12.5	5.3	8.5
191	4.0×10^{-6}	0.64	12.5	5.4	8.5
205	7.0×10^{-7}	0.6	12.5	5.1	8.1
215	6.5×10^{-7}	0.6	12.5	5.1	7.5
244	9.5×10^{-8}	0.4	12.5	3.0	5.5
256	7.5×10^{-8}	0.38	12.5	2.5	5.2
266	6×10^{-8}	0.38	12.5	1.2	5.2

Mn^{2+} sites, Mn_A^{2+} and Mn_B^{2+}, differing in their D and E values and the orientation of the ZFS tensor with respect to the crystal axes (see Table 2). Moreover, each consists of four crystallographic sites, which are related by the I_{222} symmetry of the crystal. Two possible models are consistent with these results; in the first, there are two types of tetramers, randomly distributed in the crystal, where in one

type all Mn^{2+} ions are Mn_A^{2+} ions, and in the other, all four are Mn_B^{2+} ions. Alternatively, each tetramer contains a random distribution of the two types of Mn^{2+}. The postulation of the disorder for both cases is needed to account for the insensitivity of the 110 K XRD results to the presence of two inequivalent Mn^{2+} ions (*21*). The presence of order in the first case would double the unit cell, which was not observed experimentally (*21*). As the temperature increases, the dynamic equilibrium sets in, and the single Mn^{2+} site observed at room temperature is a consequence of motional averaging between the two states. In this case, it is expected that in the ZFS tensor in the fast motion regime, i.e., at room temperature, is a weighted average of the two low-temperature tensors. The average tensor was obtained by building the ZFS matrix for each of the types from the appropriate *D*, *E*/*D*, and Euler rotation matrix using the values listed in Table 2 and an f_a of 0.38 (taken from Table 3). Then, the corresponding *D*, *E*/*D*, and Euler angles were extracted by diagonalization and compared with the experimentally determined ZFS parameters at room temperature (Table 3). For example, for site II (α, β, $\gamma + 180$; see Table 1), the average parameters are as follows: $D = 872$ MHz, $E/D = 0.109$, $\alpha = 78.5°$, $\beta = 53.6°$, and $\gamma = 231°$. Considering the experimental error, these values, except for *D*, agree reasonably with the RT values of site II ($\gamma = 45° + 180° = 225°$). A better agreement is obtained by setting f_a equal to 0.50, which yields the following: $D = 848$ MHz, $E/D = 0.115$, $\alpha = 90.4°$, $\beta = 53.0°$, and $\gamma = 228.5°$. Similar results were obtained for the other crystallographic sites within the uncertainty of $\alpha \pm 180°$ and $\gamma \pm 180°$ since α, β, and γ cannot be uniquely determined from the rotation matrix. The experimental *D* value of 728 MHz is lower than the *D* value of each of the low-temperature sites and differs significantly from the average value. This indicates that in addition to the two-state exchange there is some additional local motion that leads to the reduction of *D*. This is consistent with the observed temperature dependence of the line width of both Mn_A^{2+} and Mn_B^{2+}, which suggests the existence of a distribution within each state; namely, the minima are rather broad with that of Mn_B^{2+} being broader. As the temperature increases, this distribution decreases due to motional averaging, and this is manifested by a reduction in *D*.

The rate of conversion between the two states in the temperature range measured is $\sim 10^7 - 10^8$ s^{-1}, and the activation energy is 23.8 kJ/mol. The question that arises is what is the specific motion that leads to the modulation of the ZFS tensor. This can be induced by a low-amplitude motion of the Mn^{2+} ion itself, motion of one (or more) of the ligands, or even some motion of larger subunits that affects the coordination sphere of the Mn^{2+} ion. Any motional averaging due to molecular tumbling is ruled out because the protein is in a crystalline state.

In an attempt to identify specific residues in the Mn^{2+} site that are involved in the dynamic process, we compared the orientation of the principal axis systems of the ZFS tensors at room temperature and low temperatures with respect to the available 3D structure. Because of the symmetry of the crystal, there are four possibilities for overlaying the ZFS frames on the structure, and we chose the one where the principal axes are the closest to some local symmetry axes or bond directions. The low-temperature high resolution 3D structure (*21*) shows that the $Mn^{2+}-N$ and $Mn^{2+}-O412$ distances (the water molecule opposite the nitrogen) are slightly longer (2.233 and 2.261 Å, respectively) than the other Mn−O distances, which suggests that *z* may be along this direction. Indeed, Figure 6 shows that for one of the options (site III, Table 1) the *z* axes of Mn_A^{2+}, Mn_B^{2+}, and the RT Mn^{2+} are closer to the Mn−N direction (28−38°), while the *x* and *y* axes are closer to the equatorial plane of the three carboxylate ligands and one water molecule. The orientation of the *z* axis in all three sites is similar, and the differences between the sites can be practically expressed by a rotation about *z*. Furthermore, the orientation of the ZFS at RT (Figure 6C) is close to the average of the two low-temperature orientations, roughly obtained by a rotation of ~75° about the *z* axis. This approximately exchanges the *x* and *y* directions, from *y* being approximately along the H_2O/Asp10 direction for Mn_A^{2+} to being approximately along the Asp10/Glu8 direction for Mn_B^{2+}. The change in orientation is associated with a significant change in *E*/*D* from 0.24 to 0.145. It is therefore conceivable that the motion is associated with Asp10 and/or Asp19, which are bridging ligands to the Ca^{2+} in the S2 site, as shown in Figure 7 (*29*). The structure of concanavalin A with the bound saccharide shows a close contact of the saccharide, through a hydrogen bond, with the nitrogen of Asn14, where the adjacent carbonyl is the Ca^{2+} ligand opposite the Asp10 ligand (*29*). This is clear in Figure 7, which shows the relay between the saccharide binding and a possible displacement of the carboxylate of Asp10. It is therefore possible that the motion

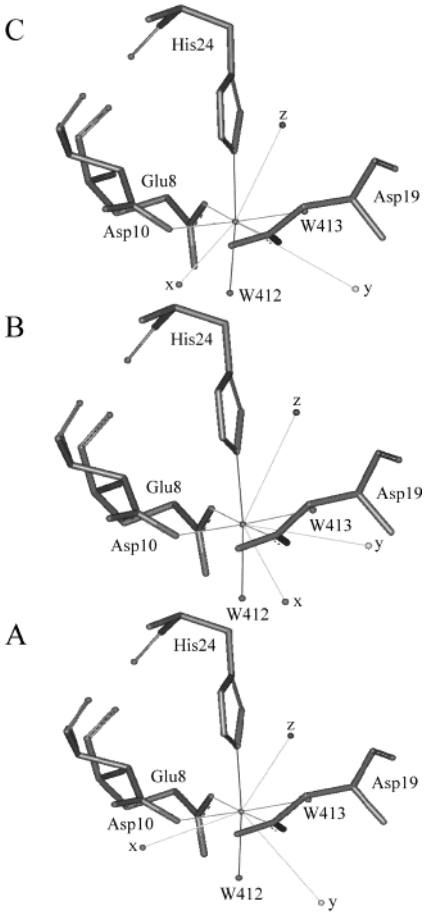

FIGURE 6: Orientation of the ZFS tensor superimposed on the 3D structure (*21*) of (A) Mn_A^{2+} at 4.5 K, (B) Mn_B^{2+} at 4.5 K, and (C) Mn^{2+} at room temperature.

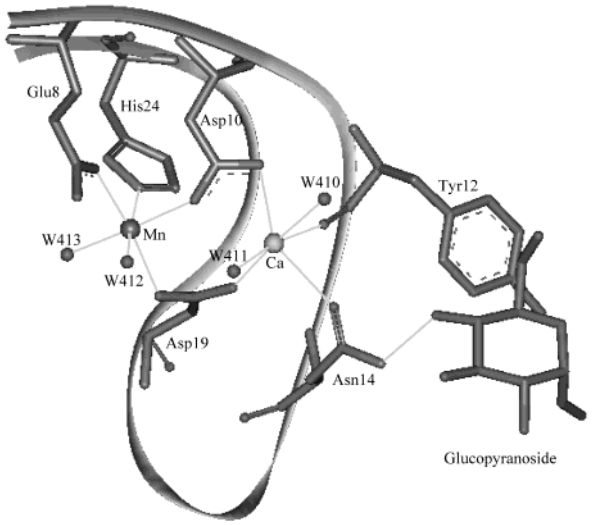

FIGURE 7: Structure of the active site of concanavalin A with the bound saccharide (*29*).

observed manifests some residual freedom, which exists to facilitate the binding of the saccharide. This then suggests that upon the saccharide binding only one site will predominate at low temperatures.

The ENDOR measurements, carried out at 4.5 K, were not sensitive to the differences between the two types of Mn^{2+}; the ENDOR spectra corresponding to Mn_A^{2+} and Mn_B^{2+} were the same (*17*). This suggests that either the Mn−H distance and orientation of the water and imidazole protons are the same for the two sites and it is one (or more) of the carboxylates that is involved in the dynamics as suggested above, or the changes are within the ENDOR line width. The XRD structure, which was measured at 110 K, does not reveal a noticeably larger temperature factor for any of the residues at the Mn^{2+} site, except that of water molecule O413 that is slightly larger. Comparison of the structures determined at 110 K and RT does not reveal a change in the Mn^{2+} binding site. In contrast, changes were detected in the loop region (Asp82, Aer117, and His121) and Lys135 and Thr196. At room temperature, they were poorly defined and the changes were attributed to freezing out of low-energy conformations (*21*). Moreover, differences involving solvent molecule movements were observed, and analysis of the residual density around the structural water oxygen leads to the suggestion of a dynamic nature of hydrogen bonding (*21*). The S2 and S1 metal sites are located at the base of a loop (residues 8−24), and the function of the metals is to stabilize the saccharide binding site. Comparison of the structure of concanavalin A with and without a bound saccharide suggested that the saccharide binding stiffens the protein around the saccharide and the metal ions (*30*−*32*), and therefore, some low-amplitude motional freedom in this region is highly conceivable.

On the basis of NMR measurements in solution, Brewster et al. (*33*) concluded that concanavalin A exists in two conformational states, one called unlocked and the other locked. The former prevails in the absence of the metal ions, while the equilibrium shifts to the locked state in the presence of the metal ions. This was latter confirmed by detailed XRD measurements, where changes inflicted by various modes of metal removal in the crystalline state allowed trapping of the metal free locked state and follow its very slow conversion to the unlocked state (*34*). They found that the changes between the two states were governed by the isomerization of a non-proline peptide bond, Ala207−Asp208, positioned between the Ca^{2+} binding site and the saccharide binding loop. The kinetics, however, was very slow, hours and days (at 5 °C) as compared to minutes in solution. This time scale is far beyond that observed in this work, thus excluding any relation to the locked versus unlocked isomerization. Moreover, the Mn^{2+} metal occupancy in our case was high (80%).

More specific information regarding the particular residues involved in the motion could be obtained, in principle, from the relation between the ZFS and atomic coordinates, namely, how bond directions dictate the ZFS direction and the magnitude of the change in the position of a ligand atom that is required to induce an observable change in the ZFS. Unfortunately, these are currently unavailable and would require extensive quantum chemistry investigations. Such calculations are currently being applied, using density functional theory (DFT), to the **g**-tensor and hyperfine interaction but scarcely to the ZFS (*36*).

Finally, we discuss the rates determined in light of dynamic processes in proteins in the crystalline state reported so far, primarily from solid state NMR. For example, the correlation time for tyrosine and phenylalanine ring flipping is in the microsecond range at room temperature (*35*, *37*). Another type of motion which involves opening and closing of a loop in the active site of triosephosphate isomerase was reported to be in the 10^4 s^{-1} range, which is significantly slower than the rate found in this work. In fully hydrated hen egg white crystalline lysozyme (*5*), the backbone amide groups show two types of motions in the range of 240−290 K: a fast one with a correlation time of ∼15 ps with an rms amplitude of 9°, which is not thermally activated, and a slow one within the range of 10^{-7}−10^{-8} s that is effectively frozen out at 250 K. The latter has been associated with the earlier observation of a conformational "glass" transition in hydrated crystalline proteins (*38*). When the dynamic properties, such as atomic mean displacements from X-ray crystallography and Mössbauer scattering, of many different proteins were plotted as a function of temperature, a biphasic behavior was observed with a broad transition around 220 K (*38*). This transition has been attributed to the freezing of atomic fluctuations dominated by anharmonic collective motions of groups of atoms. Incidentally, this temperature is close to the motion onset observed in concanavalin A. Therefore, the possibility that the two Mn^{2+} types are associated with the freezing of such collective motions into two minima with slightly different energies as manifested by the different populations of the two states at low temperatures cannot be excluded.

An interesting question that arises is whether the dynamic process that has been detected takes place in solutions as well. Unfortunately, the line width in frozen solutions is too large (35 G) due to inhomogeneous broadening and does not allow one to resolve Mn^{2+} with subtle differences as observed in a single crystal (maximum difference of 20 G) (*12*). Analysis of the Q-band EPR line shape of several forms of concanavalin A in solution in the temperature range of 276−313 K showed that the correlation times obtained were those of the molecular rotation of the entire protein molecule. Interestingly, comparison of Mn^{2+} concanavalin A and

$Mn^{2+}-Ca^{2+}$ concanavalin A showed that the former has a shorter correlation time, suggesting that the release of the Ca^{2+} from site S2 allows some local motion in the Mn^{2+} site (*39*).

CONCLUSION

Analysis of the 95 GHz EPR rotation patterns of single crystals of concanavalin A revealed that while at room temperature there is one type of Mn^{2+} in the protein, at low temperatures two types of Mn^{2+} with different ZFS parameters are clearly distinguished. Temperature dependence measurements showed a two-state exchange dynamic process, which averages the two sites at room temperature. The rate of the process is in the 10^7-10^8 s^{-1} range at 205−265 K, with an activation energy of 23.8 kJ/mol. This process is attributed to a conformational equilibrium within the Mn^{2+} binding site which freezes into two conformations at low temperatures. This work shows that the high resolution of the EPR spectrum of Mn^{2+} at high fields, combined with the sensitivity of the ZFS tensor to subtle structural changes, provides an additional tool in the study of dynamic processes in proteins.

ACKNOWLEDGMENT

We thank Dr. Linda Shimon for her help with the determination of the crystal orientations using X-ray diffraction.

REFERENCES

1. Weaver, L. H., and Matthews, B. W. (1987) *J. Mol. Biol. 193*, 189−199.
2. Gerstein, M., Lesk, A. M., and Chothia, C. (1994) *Biochemistry 33*, 6739−6749.
3. Kay, L. E. (1998) *Nat. Struct. Biol.* (NMR Suppl.), 513−517.
4. Palmer, A. G. (2001) *Annu. Rev. Biophys. Biomol. Struct. 30*, 129−155.
5. Mack, J. W., Usha, M. G., Lomg, J., Griffin, R. G., and Wittebort, R. J. (2000) *Biopolymers 53*, 9−18.
6. Rozovsky, S., and McDermott, A. E. (2001) *J. Mol. Biol. 310*, 259−270.
7. North, C. L., and Cross, T. A. (1995) *Biochemistry 34*, 5883−5895.
8. Palmer, A. G., and McDermott, A. (1996) *J. Phys. Chem. 100*, 13293−13310.
9. Hubbell, W. L., Mchaourab, H. S., Allenbach, C., and Lietzow, M. A. (1996) *Structure 4*, 779−783.
10. Likhtenshtein, G., Febbraio, F., and Nucci, R. (2000) *Spectrochim. Acta A56*, 2011−2031.
11. Schnegg, A., Fuhs, M., Rohrer, M., Lubitz, W., Prisner, T. F., and Möbius, K. (2002) *J. Phys. Chem. B 106*, 9454−9462.
12. Manikandan, P., Carmieli, R., Shane, T., Kalb (Gilboa), A. J., and Goldfarb, D. (2000) *J. Am. Chem. Soc. 122*, 3488−3494.
13. Kass, H., MacMillan, F., Ludwig, B., and Prisner, T. F. (2000) *J. Phys. Chem. B 104*, 5362−5371.
14. Rohrer, M., Prisner, T. F., Brugmann, O., Kass, H., Spoerner, M., Wittinghofer, A., and Kalbitzer, H. R. (2001) *Biochemistry 40*, 1884−1889.
15. Coremans, J. W. A., Poluektov, O. G., Groenen, E. J. J., Canters, G. W., Nar, H., and Messerschmidt, A. (1994) *J. Am. Chem. Soc. 116*, 3097−3101.
16. Coremans, J. W. A., Poluektov, O. G., Groenen, E. J. J., Canters, G. W., Nar, H., and Messerschmidt, A. (1996) *J. Am. Chem. Soc. 118*, 12141−12153.
17. Carmieli, R., Manikandan, P., Kalb (Gilboa), A. J., and Goldfarb, D. (2001) *J. Am. Chem. Soc. 123*, 8378−8386.
18. Van Gastel, M., Boulanger, M. J., Canters, G. W., Huber, M., Murphy, M. E. P., Verbeet, M. P., and Groenen, E. J. J. (2001) *J. Phys. Chem. B 105*, 2236−2243.
19. Kalb (Gilboa), A. J., Habash, J., Hunter, N. S., Price, H. J., Raftery, J., and Helliwell, J. R. (2000) *Metal Ions in Biological Systems*, Vol. 37, pp 279−304, Marcel Dekker, New York.
20. Sumner, J. B., and Howell, S. F. (1936) *J. Biol. Chem. 115*, 583−588.
21. Deacon, A., Gleichmann, T., Kalb (Gilboa), A. J., Price, H. J., Raftery, J., Brabbrook, G., Yariv, J., and Helliwell, J. R. (1997) *J. Chem. Soc., Faraday Trans. 93*, 4305−4312.
22. Meirovitch, E., Luz, Z., and Kalb, A. J. (1974) *J. Am. Chem. Soc. 96*, 7538−7541.
23. Greer, J., Kaufman, H. W., and Kalb, A. J. (1970) *J. Mol. Biol. 48*, 365−366.
24. Gromov, I., Krymov, V., Manikandan, P., Arieli, D., and Goldfarb, D. (1999) *J. Magn. Reson. 139*, 8−17.
25. Prisner, T. F., Rohrer, M., and Mobius, K. (1994) *Appl. Magn. Reson. 7*, 167−183.
26. Meirovitch, E., and Poupko, R. (1978) *J. Phys. Chem. 82*, 1920−1925.
27. Gaffney, B. J., and Silverstone, H. J. (1993) *Biological Magnetic Resonance*, Vol. 13, pp 1−55, Plenum Press, New York.
28. Weil, J. A., Wertz, J. E., and Bolton, J. R. (1994) *Electron Spin Resonance: Elementary Theory and Practical Applications*, pp 304−309, John Wiley & Sons, New York.
29. Bradbrook, G. M., Gleichmann, T., Harrop, S. J., Habash, J., Raftery, J., Kalb (Gilboa), J., Yariv, J., Hillier, I. H., and Helliwell, J. R. (1998) *Faraday Trans. 94*, 1603−1611.
30. Derewenda, Z., Yariv, J., Helliwell, J. R., Kalb (Gilboa), A. J., Dodson, E. J., Papiz, M. Z., Wan, T., and Campbell, J. (1989) *EMBO J. 8*, 2189−2193.
31. Sturtevant, M. (1977) *Proc. Natl. Acad. Sci. U.S.A. 74*, 2236−2240.
32. Jacrot, B., Cusack, S., Dianoux, A. J., and Engelman, D. M. (1982) *Nature 300*, 84−86.
33. Brown, R. D., III, Brewer, F. C., and Koenig, H. S. (1977) *Biochemistry 16*, 3883−3896.
34. Bouckkaert, J., Dewallef, Y., Poortmans, F., Wyns, L., and Loris, R. (2000) *J. Biol. Chem. 275*, 19778−19787.
35. Opella, S. J. (1986) *Methods Enzymol. 131*, 327−361.
36. Neese, F. (2003) *Curr. Opin. Chem. Biol. 7*, 125−135.
37. Torchia, D. A. (1984) *Annu. Rev. Biophys. Bioeng. 13*, 125−144.
38. Rasmussen, B. F., Stock, A. M., Ringe, D., and Petsko, G. A. (1992) *Nature 357*, 423−424.
39. Meirovitch, E., Luz, Z., and Kalb, A. J. (1974) *J. Am. Chem. Soc. 96*, 7542−7546.

BI034281+